ACS APPLIED MATERIALS & INTERFACES

www.acsami.org

Research Article

Delicately Designed Cancer Cell Membrane-Camouflaged Nanoparticles for Targeted ^{19}F MR/PA/FL Imaging-Guided Photothermal Therapy

Sha Li, Weiping Jiang, Yaping Yuan, Meiju Sui, Yuqi Yang, Liqun Huang, Ling Jiang, Maili Liu, Shizhen Chen,* and Xin Zhou*

Cite This: *ACS Appl. Mater. Interfaces* 2020, 12, 57290–57301

Read Online

ACCESS | Metrics & More | Article Recommendations | Supporting Information

ABSTRACT: Our exploration of multimodal nanoprobes aims to combine photoacoustic (PA) imaging, ^{19}F magnetic resonance (MR), and fluorescence (FL) imaging, which offers complementary advantages such as high spatial resolution, unlimited penetration, and high sensitivity to enable more refined images for accurate tumor diagnoses. In this research, perfluorocarbons (PFCs) and indocyanine green (ICG) are encapsulated by poly(lactic-*co*-glycolic acid) (PLGA) for intravital ^{19}F MR/FL/PA tri-modal imaging-guided photothermal therapy. Then, it is coated with an A549 cancer cell membrane (AM) to fabricate versatile theranostic nanoprobes (AM-PP@ICGNPs). After systemic administration, FLI reveals time-dependent tumor homing of NPs with high sensitivity, ^{19}F MRI provides tumor localization of NPs without background signal interference, and PAI illustrates the detailed distribution of NPs inside the tumor with high spatial resolution. What is more, AM-PP@ICGNPs accumulated in the tumor area exhibit a prominent photothermal effect (48.4 °C) under near infrared (NIR) laser irradiation and realize an enhanced antitumor response in vivo. These benefits, in combination with the excellent biocompatibility, make AM-PP@ICGNPs a potential theranostic nanoagent for accurate tumor localization and ultimately achieve superior cancer therapy.

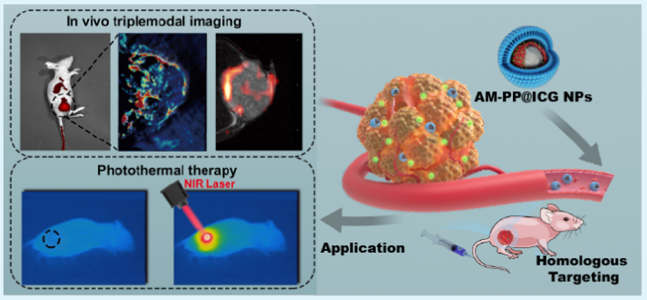

KEYWORDS: *cancer cell membrane, biomimetic nanoparticles, homotypic targeting, tri-modal imaging, photothermal tumor ablation*

INTRODUCTION

Cancer threatens the lives and health of people around the world. Visualization of the theranostic efficiency and disease progression is of great importance, which can be enabled by targeted multimodal imaging.[1−5] To achieve this goal, many imaging modalities have been explored to assess and monitor the effectiveness of cancer treatment.[6] However, every imaging technique has its unique advantages as well as drawbacks. For instance, magnetic resonance imaging (MRI) offers unparalleled spatial resolution but encounters low sensitivity; the data acquisition process is quite time-consuming.[7−9] Fluorescence imaging (FLI) allows for fast real-time scans but it suffers from low spatial resolution and poor depth penetration.[10] Photoacoustic imaging (PAI) is appropriate for vascular observation with high optical contrast and spatial resolution, but only a small area of the body can be imaged owing to the moderate laser energy.[11−13] Multimodal imaging has therefore received increasing attention as it can compensate inherent limitations of each imaging method to provide more accurate and informative images. A combination of MRI, FLI, and PAI can help to overcome each technique's limitations to present extraordinary advantages for accurate tumor diagnosis and effective antitumor treatment.[14−16]

^{1}H MRI is the most commonly used MRI, and it can provide high contrast images to show the anatomical structure and morphological changes of soft tissues. There are mainly two categories of MRI contrast agents that are widely in use, T_1 contrast agents producing hyperintense signals[17−21] and T_2 contrast agents producing hypointense signals.[22−25] However, the resulting positive signal may get fuzzy because of strong background signal interference while the obtained dark signals are always confused with intrinsic signals caused by endogenous contrast sources (blood clots and iron).[26] In contrast, there are scarcely any ^{19}F MRI signals in the background.[27−29] Fluorine mainly exists in bones and teeth in a solid form, which possess an extremely shortened T_2

Received: August 2, 2020
Accepted: November 10, 2020
Published: November 24, 2020

https://dx.doi.org/10.1021/acsami.0c13865
ACS Appl. Mater. Interfaces 2020, 12, 57290−57301

Scheme 1. Schematic Diagram of Preparation and Application of AM-PP@ICGNPs[a]

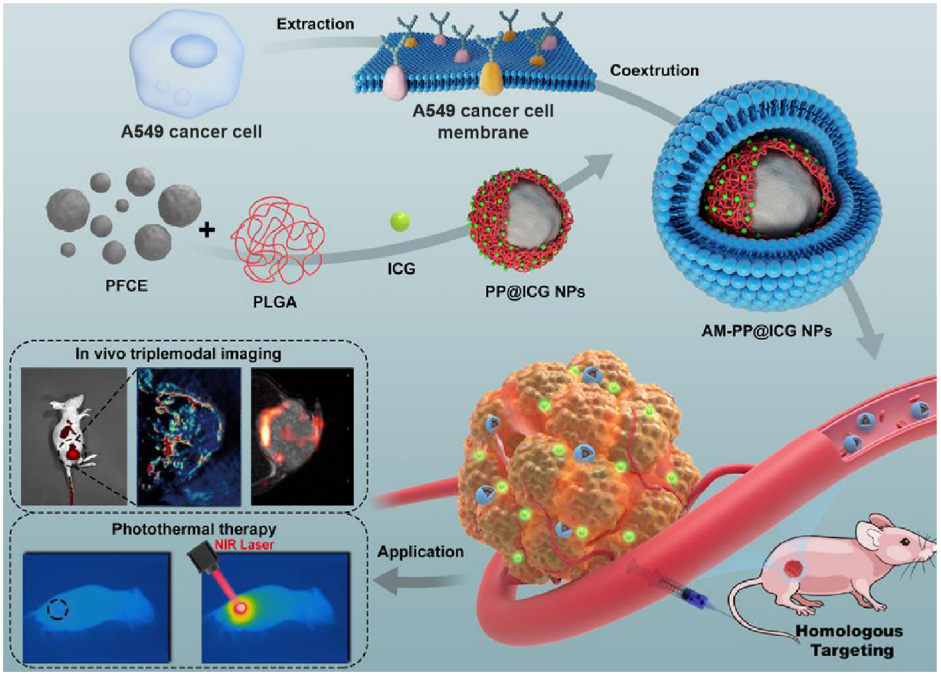

[a]Extracted A549 cell membranes were coated on prepared PP@ICGNPs by coextrusion to form AM-PP@ICGNPs. Based on homologous targeting and the EPR effect, AM-PP@ICGNPs were efficiently accumulated in the tumor, realizing excellent tri-modal ^{19}F MR/FL/PA imaging and efficient tumor ablation through photothermal effects under NIR laser irradiation.

relaxation time that is not easily detected by a conventional MRI spectrometer. Besides, fluorine offers prominent advantages over other nuclei because it has 100% natural abundance and a high gyromagnetic ratio (40.03 MHz T^{-1}), which is 94% relative to ^{1}H.[26,30] These features endow ^{19}F MRI with high sensitivity and specificity, so that it has great application potential in MR imaging.

Perfluoro-15-crown-5-ether (PFCE) is an excellent ^{19}F magnetic resonance imaging agent, with its multiple magnetically equivalent fluorine atoms it can provide a single resonance peak and eliminate any chemical shift artifact. As PFCE is lipophobic and insoluble in water, poly(lactic-*co*-glycolic acid) (PLGA) is usually used to encapsulate and stabilize PFCE for intravital applications. Thereafter, considering the loading capability of PLGA, multimodal imaging for precise detection and antitumor therapeutic efficiency, indocyanine green (ICG), a tricarbocyanine dye, which has strong absorption and emission in the near-infrared (NIR) spectrum, is incorporated into the PLGA-PFCE nanoparticles for NIR fluorescence and photoacoustic (PA) imaging. Apart from diagnostic use, ICG can also serve as a photothermal agent to effectively facilitate tumor ablation.

For tumor diagnosis and imaging-assisted therapy, there is no doubt that the effective delivery and specific targeting of theranostic agents to the tumor area is essential. To achieve this goal, many efforts have been dedicated to enhance the transportation efficiency of theranostic agents to tumors. The enhanced permeability and retention (EPR) mechanism is an important passive targeting strategy enabling nanomaterials to be retained inside tumors because of the leaky nature of tumor vessels and diminished lymphatic clearance, but it is still hard to realize efficient targeting in vivo.[31] Active targeting strategies involve surface modification with functional groups that can recognize the receptors or antigens overexpressed on the tumor surface, however, it results in complicated preparation processes. In recent years, biomimetic cell membrane-camouflaged NPs have attracted considerable attention.[32,33] It is believed that cell membrane modification confers on vesicles important surface proteins akin to original cells with unique properties. For example, RBC membrane-camouflaging endows nanoparticles with prolonged blood circulation[34−37] and stem and immune cell membranes facilitate tumor microenvironment responsive ability,[38−40] while cancer cell membranes express functional proteins or receptors (such as *N*-cadherins, epithelial cell adhesion molecules (EpCAMs), selectins, integrins, and so on),[41] which are important for various biological processes such as cell−cell adhesion and cell-matrix interaction. Thus, cancer cell membranes can be used for NP encapsulation to obtain homologous targeting ability.[42,43] It is also believed that cell membrane encapsulation can improve the stability of nanoparticles, endow nanoparticles with excellent biocompatibility, and pharmacological kinetic characteristics. These benefits make the cancer cell membrane coating an appropriate strategy to design and engineer multifunctional theranostic agents.

Taking these into account, we designed biomimetic nanoparticles camouflaged with the A549 lung cancer cell membrane (AM). This NP platform was composed of two components: (1) PFCE was encapsulated by PLGA as a core, with ICG loaded inside (PP@ICGNPs); it can generate not only ^{19}F magnetic resonance signals but also NIR fluorescence and photoacoustic signals for triple modal imaging with high contrast and spatial resolution. Under NIR laser irradiation, PP@ICGNPs can also generate heat for photothermal therapy. (2) The A549 cell membrane-based outer shell endowed PP@ICGNPs with the homologous targeting ability, promoting accumulation of PP@ICGNPs in tumors and finally enhancing diagnostic and therapeutic efficiency. After intravenous

https://dx.doi.org/10.1021/acsami.0c13865
ACS Appl. Mater. Interfaces 2020, 12, 57290−57301

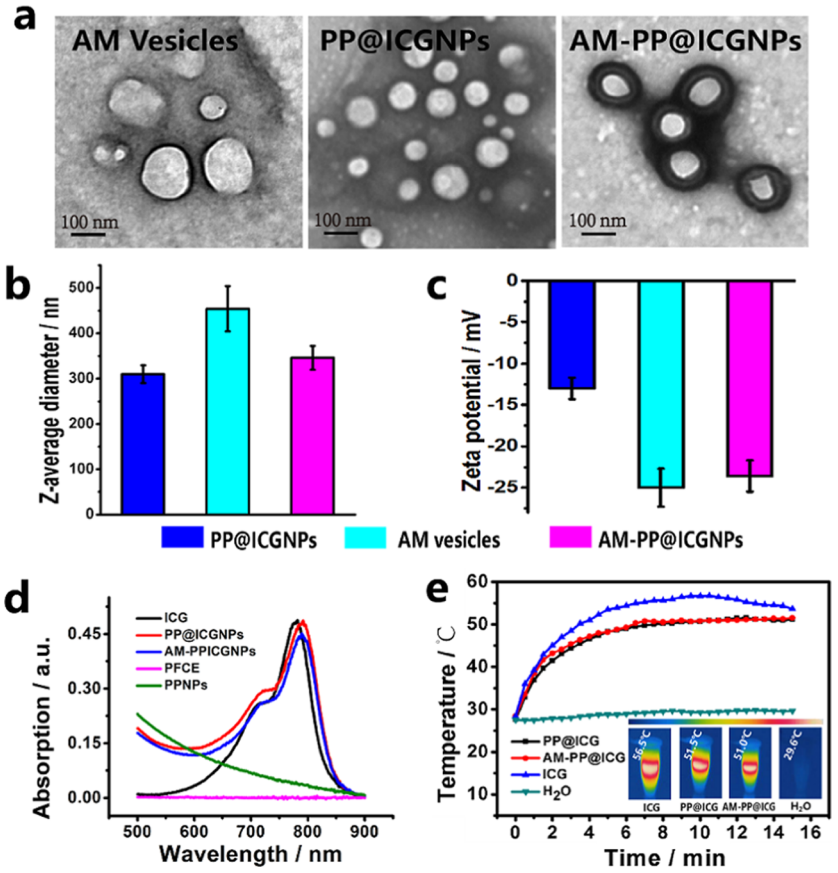

Figure 1. Characterization of AM-PP@ICGNPs. (a) TEM images of AM vesicles, PP@ICGNPs, and AM-PP@ICGNPs. (b) Hydrate particle size and (c) surface potential of AM vesicles, PP@ICGNPs, and AM-PP@ICGNPs. (d) UV−vis absorption of ICG, PP@ICGNPs, AM-PP@ICGNPs, PFCE, and PPNPs samples. (e) Infrared thermal images and temperature curves of H_2O, ICG, PP@ICGNPs, and AM-PP@ICGNPs during 765 nm laser irradiation (400 mW/cm^2).

injection of this multifunctional AM-PP@ICGNPs into the mouse model with a transplanted tumor, ^{19}F MR/fluorescence/photoacoustic triple modal imaging-guided photothermal tumor ablation was conducted, and encouraging outcomes were achieved with noticeable tumor ablation.

RESULTS AND DISCUSSION

Preparation and Characterization of AM-PP@ICGNPs.

Scheme 1 presents the preparation process of a theranostic probe, the process of functionalizing PP@ICGNPs with the A549 cancer cell membrane consists of three steps: (1) synthesizing the pristine ICG-loaded PLGA-PFCE NPs (PP@ICGNPs), (2) extracting membrane vesicles from A549 cells, and (3) coating PP@ICGNPs with the pre-extracted A549 cancer cell membrane. The protocol for encapsulating PFCE and ICG into the PLGA polymer was realized by an established water/oil/water solvent evaporation method.[44] The PFCE-loading capacity of PP@ICGNPs was calculated to be about 860% (w/w, PFCE:PLGA) as verified by ^{19}F NMR; while according to ICG's standard curve of the ultraviolet absorption spectrum (Figure S1), the content of ICG in PP@ICGNPs was determined to be about 1.2% (w/w, ICG:PLGA). Then, A549 cells were lysed through hypotonic treatment, followed by a centrifugation-based methodology to obtain bioactive membranes. The purified membranes were further dispersed by ultrasound, followed by extruding through a 400 nm filter membrane to finally fabricate A549 cell membrane-derived vesicles (AM vesicles). Later, sequential coextrusion of the sample (mixture of fresh AM vesicles and prepared PP@ICGNPs) was involved to achieve a complete cell membrane surface covering of the nanoparticles, thus forming A549 cell membrane-coated PP@ICGNPs (AM-PP@ICGNPs).

The morphologies of AM vesicles, PP@ICGNPs, and AM-PP@ICGNPs were observed by a transmission electron microscope (TEM) by negative staining. Figure 1a shows that PP@ICGNPs are exhibited as regular spheres with a 93 nm diameter. After mechanical extrusion with AM vesicles, a light gray ring emerges outside the white spherical core. The thickness of the outer ring is about 7.5 nm; this dimension is consistent with the cytomembrane evaluation reported in the literature.[45] The TEM results indicate successful coverage of PP@ICGNPs in a cell-membrane structure. Such encapsulation also give rise to an increase in the hydrate particle size (Figures 1b and S2), where AM-PP@ICGNPs are 356 nm in diameter and PP@ICGNPs are only 310 nm. Besides, the zeta potential (Figure 1c) of the PP@ICGNPs is changed from −13.2 to −23.4 mV upon fusing with AM vesicles, which appears to be similar to that of pure AM vesicles (−24.8 mV). Collectively, these results demonstrate the successful cell membrane covering on PP@ICGNPs.

Indocyanine green (ICG) is a fluorescent dye that is widely used in clinics because of excellent near-infrared (NIR) absorption performance. ICG has been extensively explored for theranostic applications, including photothermal therapy, photoacoustic imaging, and fluorescence imaging. After being

https://dx.doi.org/10.1021/acsami.0c13865
ACS Appl. Mater. Interfaces 2020, 12, 57290−57301

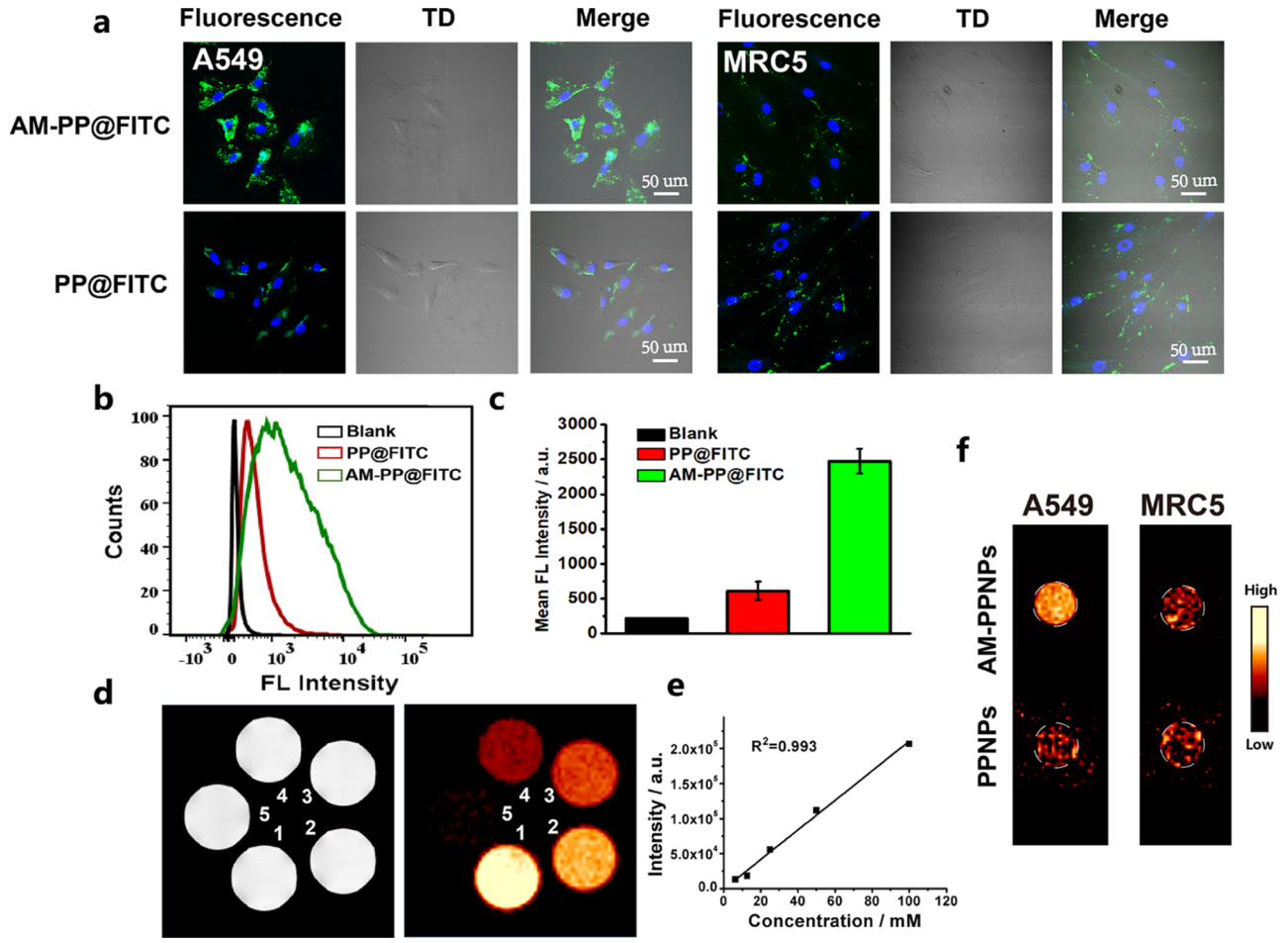

Figure 2. In vitro cellular uptake assays of AM-PPNPs. (a) CLSM imaging of A549 cells and MRC-5 cells incubated with PP@FITCNPs and AM-PP@FITCNPs for 6 h. DAPI was used to label cell nuclei. (b) Flow cytometry analysis and (c) quantification of A549 cells after co-incubation with PP@FITCNPs and AM-PP@FITCNPs. (d) ^{1}H MRI images (left) and ^{19}F MRI images (right) of AM-PPNPs at different concentrations. (1−5): C_F = 100, 50, 25, 12, and 6 mM. (e) Relationship between ^{19}F MRI signal intensities and AM-PPNPs concentrations. (f) ^{19}F MRI of A549 and MRC-5 cells incubated with PPNPs and AM-PPNPs.

encapsulated by the cancer cell membrane, the optical and photothermal properties of AM-PP@ICGNPs were studied. The ultraviolet−visible (UV−vis) absorption spectra (Figure 1d) show that there is no significant UV absorption of PFCE and PPNPs, while the absorption peaks of PP@ICGNPs and AM-PP@ICGNPs are both located at 786 nm, the absorption peak of ICG is 780 nm. This indicates that ICG is successfully loaded into nanoparticles. Compared to free ICG, the absorption peaks of PP@ICGNPs and AM-PP@ICGNPs both slightly red-shifted from 780 to 786 nm, which may correspond to the formation of weak aggregation of closely packed ICG inside the nanoparticles. The photothermal capacity of AM-PP@ICGNPs is assessed in an aqueous dispersion. As shown in Figure 1e, under continuous 765 nm NIR laser irradiation (400 mW/cm^2, 15 min), the temperatures of free ICG, PP@ICGNPs, and AM-PP@ICGNPs solutions at the same concentration rise to 56.5, 51.0, and 51.5 °C, respectively, whereas the maximum temperature of PBS only increases to 29.6 °C. Noticeably, the temperature of free ICG is slightly decreased after 10 min laser irradiation, which may be caused by its instability in the aqueous solution as well as heat dissipation, while PP@ICGNPs and AM-PP@ICGNPs can maintain the high temperature even after 15 min irradiation. Besides, Figure S3 shows the photothermal stability of AM-PP@ICGNPs, after five cycles of 765 nm NIR irradiation (400 mW/cm^2, 6 min on and 9 min off), the photothermal stability of AM-PP@ICGNPs is unchanged. The superior temperature rise and improved photostability of AM-PP@ICGNPs is of great importance for intravital photothermal therapy.

Homologous Targeting of AM-PPNPs. It is reported that cancer cell membrane coverage personalized nanoparticles with homotypic targeting performance due to the retained cell membrane proteins. To prove that AM-PPNPs were successfully functionalized by cancer cell membrane adhesion proteins, we performed SDS-PAGE (sodium dodecyl sulfate polyacrylamide gel electrophoresis) to characterize the protein compositions of A549 cancer cells, AM vesicles, and AM-PPNPs (Figure S4). The comparable protein profiles between AM-PPNPs and A549 cancer cells evidence the existence of A549 cancer cell membrane proteins in our obtained AM-PPNPs sample. The above results demonstrate that AM-PPNPs can retain biomimetic properties of A549 cancer cell membranes.

After confirming that nanoparticles are successfully coated with the cell membrane, we further conducted cellular uptake experiments to explore the homologous targeting ability of AM-PPNPs toward lung cancer A549 cells using a confocal

https://dx.doi.org/10.1021/acsami.0c13865
ACS Appl. Mater. Interfaces 2020, 12, 57290−57301

laser scanning microscope (CLSM). A549 cells were coincubated with FITC-loaded AM-PPNPs (AM-PP@FITCNPs) for different times. Figure S5 indicates that the uptake of AM-PP@FITCNPs by A549 cells is a time-dependent process. AM-PP@FITCNPs are mainly accumulated in the cytoplasm, maximum accumulation is achieved when the incubation time is up to 6 h. Then, CLSM of A549 cells incubated with bare PP@FITCNPs and AM-PP@FITCNPs for 6 h were conducted. Compared to bare PP@FITCNPs, AM-PP@FITCNPs show strong affinity for A549 cells as there is brighter green fluorescence in the cytoplasm (Figure 2a), indicating a markedly promoted cell internalization process. Quantitation of nanoparticles swallowed in cells was then employed by flow cytometry analysis. In Figure 2b,c, AM-PP@FITCNPs show approximately 4-fold higher cellular uptake than that of PP@FITCNPs. Additionally, we evaluated the targeting specificity of AM-PP@FITCNPs between the lung cancer A549 cell and human embryonic lung fibroblasts MRC-5 cell. CLSM images show that both AM-PP@FITCNPs and bare PP@FITCNPs exhibit no difference but negligible green fluorescence in MRC-5 cells (Figure 2a).

It is noteworthy that PFCE residing in the core could provide high ^{19}F magnetic resonance signals. As shown in Figure 2d, significant ^{19}F MR "hot-spot" images are detected for different concentrations of the AM-PPNPs solution, and there exists a linear correlation between the ^{19}F MRI signal intensity and fluorine concentration (Figure 2e), which can provide reliable signal quantification. In vitro ^{19}F MRI experiments were then carried out. A549 cells and MRC-5 cells were incubated in a serum-free medium containing AM-PPNPs and PPNPs for 6 h, respectively; after purification, cell suspensions were prepared and placed into an NMR tube (10 mm in diameter) for ^{19}F MRI tests. Figure 2f shows that the ^{19}F MRI signal intensity of A549 cells incubated with AM-PPNPs is obviously stronger than that of other control groups. This indicates that due to the encapsulation of the cancer cell membrane, AM-PPNPs possess significant homologous targeting adhesion toward their source cancer cells.

To detect the stability of the core−shell particle structure during endocytosis, PPNPs were loaded with a hydrophobic FITC (E_x = 490 nm, E_m = 520 nm), while the outer membrane was tagged with lipophilic DiI (E_x = 549 nm, E_m = 565 nm). The resulting dual-fluorophore-labeled nanoparticles (AM@DiI-PP@FITCNPs) were incubated with A549 cells and visualized using a fluorescence microscope (Figure S6). The result shows that nanoparticles are mainly accumulated in the cytoplasm, the green fluorescence of the labeled PLGA polymer and the red fluorescence of the labeled covering membrane exhibit large areas of overlap, indicating that AM-PPNPs can maintain an intact core−shell structure upon cellular endocytosis.

In Vitro Photothermal Cytotoxicity of AM-PP@ICGNPs. Given the promising photothermal effect of AM-PP@ICGNPs in aqueous solution, we further investigated the cytotoxicity and in vitro photothermal therapy efficacy of AM-PP@ICGNPs. A549 cells were incubated in PBS, ICG, PP@ICGNPs, and AM-PP@ICGNPs, respectively, followed by exposure to a near-infrared laser with 765 nm wavelength (1000 mW/cm^2) for 10 min. Figure 3a shows that AM-PP@ICGNPs-treated cells under the irradiation area are shrinked and become smaller, which are involved in the apoptosis process, while in the nonirradiated region, the cell morphology

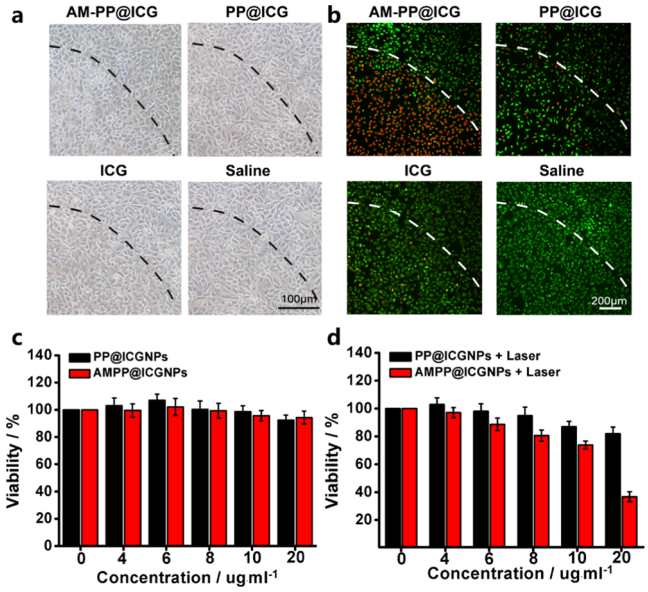

Figure 3. In vitro cellular photothermal toxicity of AM-PP@ICGNPs. (a) White light and (b) CLSM images of calcein-AM/PI labeling of A549 cells with PBS, ICG, PP@ICGNPs, and AM-PP@ICGNPs incubation, followed by exposure to a near-infrared laser with 765 nm wavelength (1000 mW/cm^2) for 10 min. The MTT assay of A549 cells treated with PP@ICGNPs or AM-PP@ICGNPs at various doses (d) with and (c) without laser irradiation (1000 mW/cm^2) for 5 min.

is normal. In contrast, A549 cells treated with PBS, ICG, and PP@ICGNPs fail to evoke apoptosis with or without irradiation. Photothermal ablation for cell apoptosis was further validated by CLSM. For viable and dead cell differentiation, calcein-AM and propidium iodide (PI) were utilized to label A549 cells. Figure 3b shows that cells incubated with AM-PP@ICGNPs within the NIR irradiation area display strong red fluorescence, while the neighboring cells that are unexposed to light emit bright green fluorescence, implying that cells were severely damaged because of the strong photothermal effect induced by AM-PP@ICGNPs. In sharp contrast, cells incubated with PBS, ICG, and PP@ICGNPs show green fluorescence both inside and outside the light spot, implying good cell compatibility under these conditions. To sum up, these results consistently show that AM-PP@ICGNPs can preferentially accumulate in A549 cells and good photothermal cytotoxicity can be induced upon NIR laser irradiation.

To quantitatively evaluate the photothermal efficacy of AM-PP@ICGNPs, the MTT assay was performed. In Figure 3c, both PP@ICGNPs and AM-PP@ICGNPs show negligible cytotoxicity up to 20 μg/mL dose of ICG against A549 cells in the absence of light irradiation, while dose-dependent cytotoxicity is observed with both PP@ICGNPs and AM-PP@ICGNPs incubation under laser irradiation (Figure 3d). AM-PP@ICGNPs show stronger cytotoxicity than PP@ICGNPs. The MTT assay reveals that about 38% of the tumor cells treated with AM-PP@ICGNPs remain alive after NIR irradiation at the ICG dose of 20 μg/mL, while the viability of the PP@ICGNPs group is ≈90%. Taken together, these results suggest the enhanced homologous targeting ability of AM-PP@ICGNPs toward A549 cells, paving the way for effective photothermal tumor cell ablation.

In Vivo ^{19}F MR/PA/FL Tri-Modal Imaging. The ideal nanoprobe should effectively target the tumor sites and be

https://dx.doi.org/10.1021/acsami.0c13865
ACS Appl. Mater. Interfaces 2020, 12, 57290−57301

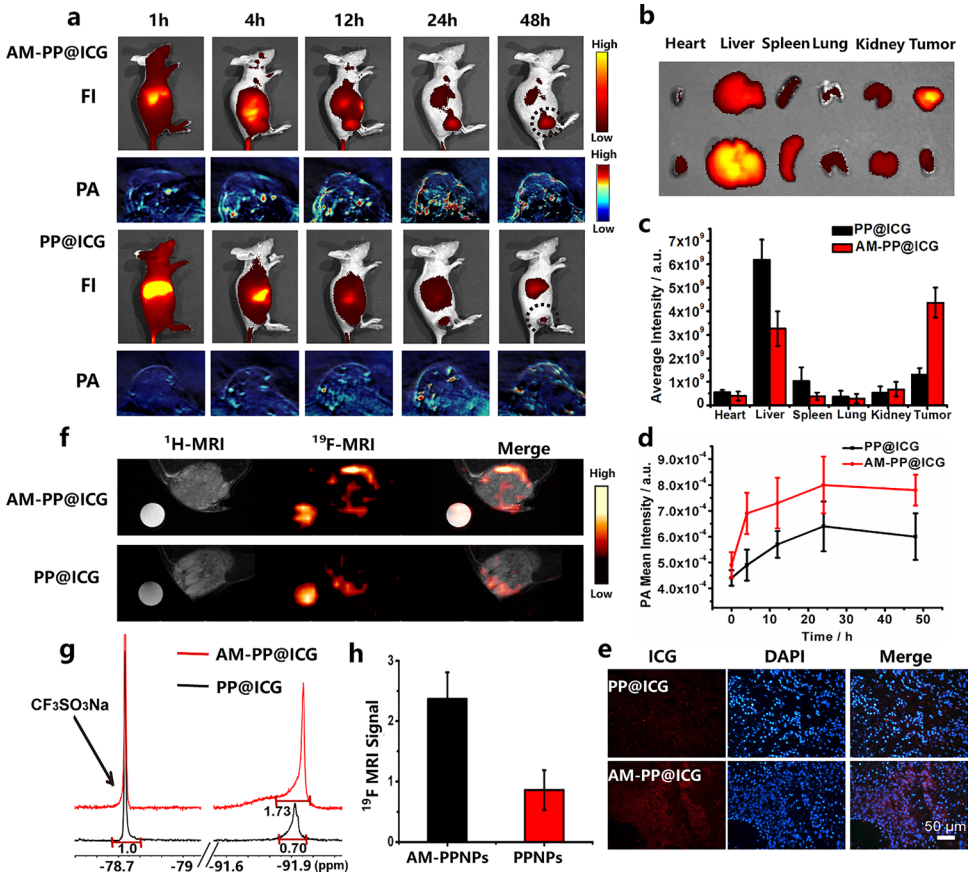

Figure 4. In vivo targeted tri-modal imaging of AM-PP@ICGNPs. (a) In vivo FL and PA imaging after intravenous injection of PP@ICGNPs and AM-PP@ICGNPs at various times. (b) Fluorescence imaging and (c) fluorescence intensity measurements of isolated organs and tumors at 24 h postinjection of different NPs. (d) PA signal intensity inside the tumor changes over time. (e) Histological staining of tumor tissue sections. Cell nuclei were stained by DAPI. (f) ^{19}F MRI of the A549 tumor tissue suspension at 24 h postinjection of PP@ICGNPs and AM-PP@ICGNPs. (g) ^{19}F NMR spectra of tumor tissue suspension (14 mg/mL) and (h) ^{19}F MRI signal ratio between the tumor and external standard postinjection of PP@ICGNPs and AM-PP@ICGNPs.

detected for accurate cancer treatment. The aforementioned cellular imaging results prompted us to verify the in vivo targeting ability of AM-PP@ICGNPs. First, we gauged the time-lapsed biodistribution of AM-PP@ICGNPs and bare PP@ICGNPs (0.2 mg/mL dose of ICG) in model mice bearing A549 tumor xenografts. They were illuminated using an IVIS Spectrum imaging system (E_x: 745 nm; E_m: 840 nm) and the emission was obtained. In Figure 4a, both AM-PP@ICGNPs and bare PP@ICGNPs predominantly accumulate in the liver within 1 h after injection, which is the primary phagocyte-enriched reticuloendothelial system (RES). The signals gradually diminished as time passed and accumulated in tumor tissue. Finally, a weak fluorescence signal was detected inside the tumor 24 h postinjection of PP@ICGNPs, which was presumably due to the enhanced penetration and retention (EPR) effect of nanoparticles. On the contrary, by virtue of the cancer cell membrane functionalization, AM-PP@ICGNPs possess both passively and actively targeting capabilities, resulting in a significantly intensive fluorescence signal in the tumor at 24 h postinjection. It is particularly noteworthy that the strong fluorescence intensity of AM-PP@ICGNPs in the tumor still remains steady at 48 h, while there is a significant reduction of the signal between 24 and 48 h after PP@ICGNPs injection. This implies that AM-PP@ICGNPs can successfully reach the tumor and remain for a prolonged time. To further reveal nanoparticle biodistribution in the living body, the mice were euthanized at 24 h after injection, and major organs and tumors were collected for fluorescence imaging under the IVIS Spectrum imaging system (Figure 4b). Evidently, the fluorescence intensity inside the tumor of AM-PP@ICGNPs injected mice is 3.6-fold higher than that of PP@ICGNPs injected mice (Figure 4c). On the other hand, the liver and spleen accumulation of AM-PP@ICGNPs is much lower than that of PP@ICGNPs.

Photoacoustic imaging emerges as a novel noninvasive imaging modality that combines the merits of deep penetration as well as unique sensitivity. Figure 4a depicts in vivo PA imaging after tail vein injection of AM-PP@ICGNPs and PP@ICGNPs. Prominent photoacoustic signals of AM-PP@ICGNPs emerge and scatter throughout the tumor. The total signal intensity slowly increases over time and reaches the maximum at 24 h postinjection. This result is in accordance with the fluorescence imaging experiment. The PA signal intensity of AM-PP@ICGNPs inside the tumor at 24 h is 1.4-fold higher than that of PP@ICGNPs (Figure 4d), which signifies the tumor homing ability of AM-PP@ICGNPs via the cancer cell membrane-mediated homologous targeting effect. We further examined tumor slices using CLSM to visualize the nanoparticles in tumors at 24 h postinjection (Figure 4e). Co-registration of cell nuclei (DAPI) stains enables the qualitative visual assessment of the nanoparticle burden. The tumor slices reveal a significantly enhanced fluorescence signal of AM-PP@

https://dx.doi.org/10.1021/acsami.0c13865
ACS Appl. Mater. Interfaces 2020, 12, 57290−57301

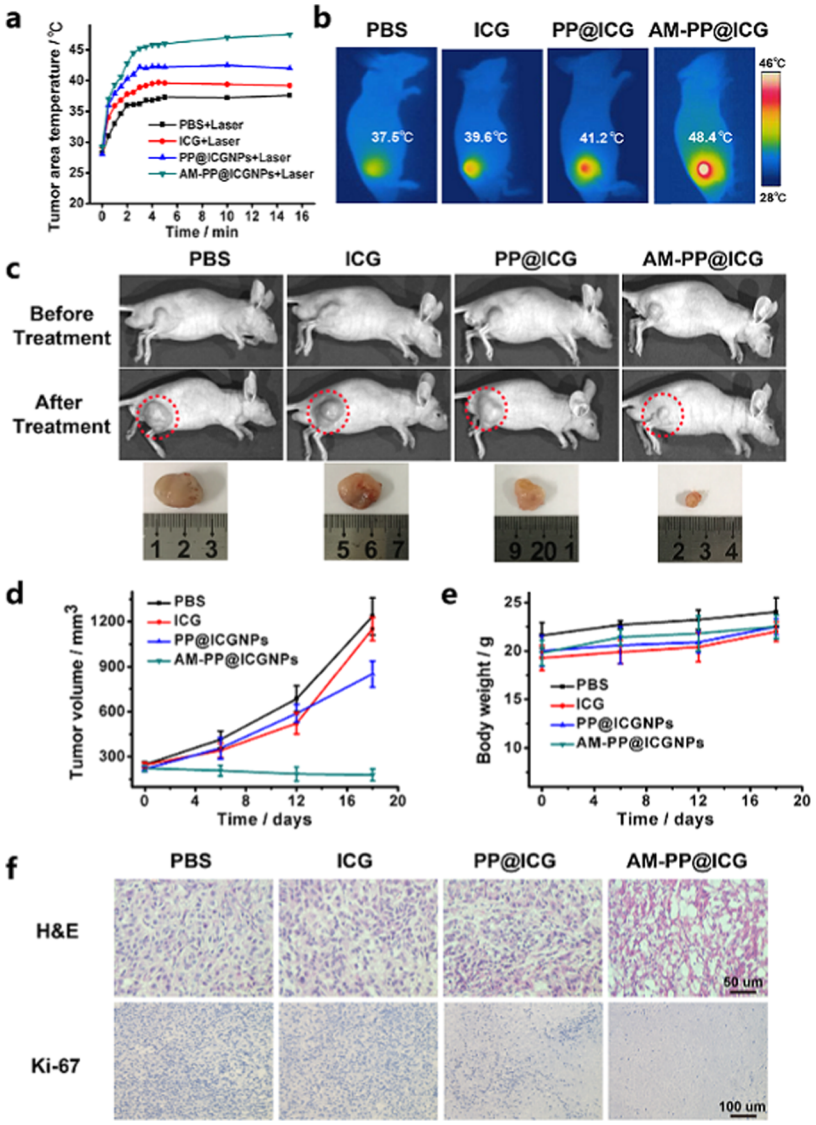

Figure 5. Photothermal tumor ablation efficiency of AM-PP@ICGNPs. (a) Tumor site temperature changes over time after tail vein injection of PBS, ICG, PP@ICGNPs, and AM-PP@ICGNPs. (b) Thermal infrared images of xenograft tumor mice after intravenous injection of PBS, ICG, PP@ICGNPs, and AM-PP@ICGNPs under 765 nm NIR laser irradiation. (c) Representative pictures of xenograft tumor mice and their excised tumors after treatments. (d) Tumor size and (e) body weight changes of mice versus time of each treatment group. (f) Tumor sections with H&E and Ki-67 staining.

ICGNPs injected mice, proving its improved accumulation toward the tumor.

^{19}F MRI generates "hot-spot" images without any endogenous background signal, which offers advantages to obtain a higher signal to noise ratio. With PFCE included inside the nanoprobe, ^{19}F MR images were also recorded after 24 h AM-PP@ICGNPs (20 mg/mL, 200 μL) postinjection using a 9.4 T MR instrument. As shown in Figure 4f, an external standard tube containing PP@ICGNPs samples is placed by the torso of the mice and ^{1}H/^{19}F MR images are acquired. Visually, an intense ^{19}F MRI hot-spot signal located at the tumor periphery in AM-PP@ICGNPs intravenously injected mice is observed, while there are only few ^{19}F-positive signals in the tumor of PP@ICGNPs injected mice, implying the triumphant tumor accumulation of AM-PP@ICGNPs. Quantitatively, the region of interest (ROI) analysis within the tumor volume was carried out (Figure 4h) by comparison with the external NMR tube placed beside the mouse torso. The ^{19}F signal intensity of the standard sample is set to be 1.0.[46] The intratumoral ^{19}F MRI intensities of nanoparticles are thus calculated to be 0.84 and 2.37 for PP@ICGNPs and AM-PP@ICGNPs, respectively. Later, ^{19}F NMR spectra of the excised tumor (24 h postinjection) are measured and the result is shown in Figure 4g. With CF_3SO_3Na as the internal reference whose chemical shift is set to be −76.55 ppm and the intensity to be 1.0, the integrals of the ^{19}F NMR signal at −94 ppm are measured to be 1.73 and 0.7 for tumors containing AM-PP@ICGNPs and PP@ICGNPs, respectively. These quantitative differences are consistent with in vivo imaging assays, where the FLI, PAI and ^{19}F MRI signal intensities of AM-PP@ICGNPs in tumors are higher than that of bare PP@ICGNPs.

A longer blood circulation also ensures sufficient accumulation of nanoparticles in the tumor. Therefore, the blood circulation profiles of AM-PP@ICGNPs, bare PP@ICGNPs, and ICG were investigated. After tail vein injection into laboratory mice, blood was withdrawn from the orbital venous

https://dx.doi.org/10.1021/acsami.0c13865
ACS Appl. Mater. Interfaces 2020, 12, 57290−57301

plexus at regular intervals for fluorescence intensity measurement (Figure S7). The half-time of AM-PP@ICGNPs is calculated to be about 9.8 h, which is about 1.7 times that of PP@ICGNPs and 3 times that of ICG molecules. Obviously, the cancer cell membrane modification can effectively enhance circulation times of PP@ICGNPs.

Therefore, thanks to the cancer cell membrane coating that offers PP@ICGNPs the capability to preferentially accumulate at tumor sites, and triple modal ^{19}F MR/FL/PA imaging is realized using AM-PP@ICGNPs as the contrast agent in our study. ^{19}F MRI, enabled by the PFCE liquid core, provides more accurate anatomical information of tumors but its sensitivity could be a worrying problem. As a complementarity, FL imaging is sensitive for fast real-time scan, however, it suffers from low penetration and scattering-limited spatial resolution. Thus, it is unreliable to quantify signals of tissues located at different depths. Besides, PA imaging possesses high spatial resolution and can vividly reveal the heterogeneous intratumoral distribution of nanoparticles but it is difficult to perform whole-body imaging. Integrating the complementary advantages of those three imaging modalities in one therapeutic schedule can triumphantly provide comprehensive diagnosis of tumors.

In Vivo Photothermal Therapy. Since AM-PP@ICGNPs is proven to have effective tumor homing ability and excellent photothermal conversion efficiency, we thus tested the potential of AM-PP@ICGNPs for in vivo therapy. A total of 20 nude mice were used; when the tumors reached a diameter of about 4 mm, they were randomly allocated into four groups. To avoid skin burns, the power density of the 765 nm NIR laser was set at 400 mW/cm^2. In the treatment group, all of the mice were intravenously injected with AM-PP@ICGNPs (200 μL, 500 μg/mL of ICG), followed by NIR irradiation for 15 min. In the other three control groups including injection with PP@ICGNPs, ICG, and PBS, the mice were irradiated in the same way. Infrared imaging devices were used to detect the tumor surface temperature. In Figure 5a, the tumor temperature of mice with AM-PP@ICGNPs injection shows a rapid increase and reaches the maximum of 48.4 °C after laser irradiation (Figure 5b). The generated temperature rise (above 42 °C) was competent enough to damage tumor cells.[47] By contrast, the tumor surface temperature showed little change for mice injected with PP@ICGNPs (41.2 °C), ICG (39.6 °C), and PBS (37.5 °C) under irradiation with the same parameter. This implies that due to the cancer cell membrane coating, accumulation of intravenously administered AM-PP@ICGNPs in tumors can be promoted and significant heat can be generated under NIR irradiation. Then, the in vivo antitumor effect of photothermal therapy was evaluated over 18 days after three periods of treatment (Figure 5c). Owing to the higher accumulation in tumors and higher photothermal temperature of AM-PP@ICGNPs, significantly retarded tumor growth (Figure 5d) was observed for AM-PP@ICGNPs injected mice (86% reduction of tumor volumes after treatment). In comparison to the enlarged tumor sizes of the PP@ICGNPs group (388%), ICG group (468%), and blank group (498%), AM-PP@ICGNPs show a superior antitumor effect.

Afterward, tumors were extracted and sectioned for hematoxylin and eosin (H&E) staining after treatments (Figure 5f). Significant necrosis appeared in the tumor tissues of AM-PP@ICGNPs-treated mice, whereas the other three groups showed no obvious necrosis. Additionally, Ki-67 assays were carried out to investigate the tumor cell proliferation level. The negative result of Ki-67 staining in AM-PP@ICGNPs-treated tumor tissues indicates that AM-PP@ICGNPs can effectively inhibit tumor proliferation. These histological analyses suggest that, owing to the natural functionalities of donor cell membranes, AM-PP@ICGNPs outperformed PP@ICGNPs and ICG in cancer photothermal therapy through enhanced tumor accumulation.

We next sought to evaluate the biosafety of AM-PP@ICGNPs in vivo. During the observational period, there were no abnormalities in the daily behavior and body weight of mice (Figure 5e), demonstrating that the designed therapeutic strategy was reasonably well tolerated. After the entire treatment, the mice were sacrificed and major organs including the spleen, liver, kidneys, heart, and lungs were extracted for histological analysis (Figure S8). The result does not reveal any significant histopathological abnormalities or lesions between the AM-PP@ICGNPs injected mice and the control groups, indicating the favorable biocompatibility of the AM-PP@ICGNPs-mediated photothermal therapy. Additionally, blood biochemistry analyses were carried out (Figure S9); and the result shows that there is no abnormal expression of key functional indicators of the liver and kidneys (aspartate aminotransferase (AST), alanine aminotransferase (ALT), creatinine (CRE), and blood urea nitrogen (BUN)) among all the four groups, indicating that AM-PP@ICGNPs possess negligible side effects at the administered dose.

CONCLUSIONS

Briefly, we have designed cancer cell membrane-coated nanoprobes with an enhanced targeting ability to homologous tumors, and they can achieve tri-modal imaging (^{19}F MRI/FLI/PAI)-guided photothermal therapy under NIR laser irradiation. Lung cancer A549 cell membrane coating endowed PP@ICGNPs with effective homologous targeting ability, excellent biocompatibility, and long blood circulation, which remarkably promote the tumor targeting and retention of PP@ICGNPs. Tri-modal imaging was realized to get accurate tumor observation, where FLI shows time-dependent tumor accumulation of NPs with high sensitivity, ^{19}F MRI provides tumor localization of NPs without any background signal interference, and PAI illustrates the heterogeneous distribution of NPs inside the tumor with high spatial resolution. On account of the enhanced enrichment of AM-PP@ICGNPs in tumors and their promising photothermal effect, in vivo photothermal therapy was carried out upon mild localized laser irradiation (765 nm, 400 mW/cm^2, 15 min) and obvious tumor growth inhibition was achieved in AM-PP@ICGNPs administered mice. In a word, the versatile biomimetic theranostic nanoprobe AM-PP@ICGNPs hold great potential for multimodality imaging-guided photothermal tumor ablation.

MATERIALS AND METHODS

Materials. Poly(lactic-*co*-glycolic acid) (PLGA) (lactide:glycolide = 50:50, M_W = 7000) was purchased from Sigma-Aldrich. Indocyanine Green (ICG), perfluoro-15-crown-5-ether (PFCE, 99%, M_W = 580.08), poly(vinyl alcohol) (PVA, 99%, M_W = 30 000−70 000 Da), and fluorescein isothiocyanate isomer (FITC) were purchased from J&K Scientific Ltd. DiI was purchased from Yeasen Biotech Co., Ltd.

Synthesis of PPNPs. PLGA particles containing PFCE were prepared based on the water/oil/water solvent evaporation technique.

https://dx.doi.org/10.1021/acsami.0c13865
ACS Appl. Mater. Interfaces 2020, 12, 57290−57301

Briefly, 100 μL of PFCE was added to 10 mg of PLGA dissolved in dichloromethane (500 μL), into which 5 mL of 4% PVA solution (w/v) was then added. After well blended, the mixture was placed on ice and sonicated for 40 min in total, with 1 s-on, 2 s-off, and 20% power output. The homogenized emulsion was stirred later for 4 h in open air at room temperature to vaporize organic solvents. The product was then centrifuged (14 000 rpm) at 4 °C for 15 min, washed several times using pure water to remove PVA, and then collected the final product, PPNPs, and stored in pure water at 4 °C for future use. ICG or FITC-labeled PPNPs were prepared by mixing 1 mg of ICG or 1 mg of FITC (dissolved in 100 μL of methanol) with PLGA solution and purified to remove the free molecule.

Preparation of A549 Cell Membrane Vesicles. A previously reported extrusion approach was used to prepare the membrane material.[34] The harvested A549 cells were treated with hypotonic pH = 7.4 Tris HCl buffer (2 mM $MgCl_2$, 10 mM KCl, and 100 μL of the protease inhibitor without EDTA were mixed with 10 mL of the solution) at 4 °C for 1 h, followed by sonication for 2 min, with 2 s-on, 5 s-off, and 20% power output to allow complete lysis of cells. The lysed cell suspension was first centrifuged at low speed (500 *g*) for 15 min to precipitate the intracellular impurities. The supernatants were then collected and ultracentrifuged at 100 000 *g* for 1 h (Optima L-100 XP Ultracentrifuge, BECKMAN COULTER) to get the cell membrane vehicle's pellet, followed by washing three times with PBS. The pellet was then suspended in PBS for further use. The surface potential and hydrodynamic size of AM vesicles were examined by a DynaPro dynamic light scatterer (DLS) (Malvern Corp, U.K. ZEN3690).

Preparation of AM-PP@ICGNPs. PP@ICGNPs were added dropwise into the AM vesicles' solution under ultrasonication. The mass ratio of AM vesicles to PP@ICGNPs was 1:1. The mixed solution was squeezed through a filter with a 400 nm aperture repeatedly to process the membrane coverage for PP@ICGNP cores. The resulting AM-PP@ICGNPs were purified through centrifugation several times and finally stored in PBS. The zeta potential and hydrate particle size of AM-PP@ICGNPs were determined by DLS. The surface morphology of AM vesicles, PP@ICGNPs, and AM-PP@ICGNPs were observed by a TEM (100 kV, HITACHI H-7000FA, Japan) with phosphotungstic acid-mediated negative staining.

In Vitro Cellular Uptake. A549 cells and MRC-5 cells were seeded in a 6-well plate with a coverslip placed at the bottom; the cell density was about 2×10^4 per well. Cells were incubated overnight until they adhered to the wall, and then the culture medium was removed. Cells were then treated with AM-PP@FITCNPs and bare PP@FITCNPs for 6 h. After washing with PBS three times, the cell nucleus was stained with DAPI. The cells were washed again with PBS, followed by fixation in 4% paraformaldehyde. Coverslips were finally mounted onto glass slides and imaged by a confocal laser scanning microscope (A1R/A1, Nikon, Japan).

Cells were harvested after incubation and flow cytometer analysis (BD LSRFortessa) was performed to record the fluorescence histograms of FITC.

In Vitro Photothermal Toxicity of AM-PP@ICGNPs. A549 cells were seeded into a 6-well chamber and the cell concentration was controlled to be 2×10^4 cells per well. After 12 h of attachment, the serum-free medium containing AM-PP@ICGNPs, PP@ICGNPs, ICG, and PBS was added for further 6 h incubation. Then, a 765 nm NIR laser (power density is 1000 mW/cm^2) was employed to illuminate cells for 10 min. After irradiation, the cell morphology was observed using an optical microscope. Then, the viable and dead cells were, respectively, labeled with calcein-AM and PI and visualized under a confocal laser scanning microscope (A1R/A1, Nikon, Japan).

The MTT assay was performed to evaluate the cytotoxicity of different nanoparticles. Briefly, seeded A549 cells into a 96-well chamber with 200 μL of the culture medium, controlled the cell concentration to be 1×10^4 cells per well, and incubated the cells overnight for attachment. 200 μL of the serum-free medium with different concentrations of AM-PP@ICGNPs and PP@ICGNPs (4, 6, 8, 10, 20 μg/mL ICG) were added to the well, followed by 4 h co-incubation. A 765 nm NIR laser (1000 mW/cm^2) was applied to illuminate cells for 5 min. Thereafter, 200 μL of the culture medium containing 0.5 mg/mL MTT was added to the wells. After 4 h co-incubation with cells, 200 μL of DMSO was used to dissolve the blue crystals produced by live cells per well. The absorbance was measured at 490 nm by an ELISA plate reader (Spectra MAX 190, Molecular Devices).

In Vivo Homologous Targeting of AM-PP@ICGNPs. When the tumors had grown to about 0.7 cm in diameter, six nude mice were averagely allocated into two groups. Mice were intravenously injected with 200 μL of AM-PP@ICGNPs and bare PP@ICGNPs with a concentration of 200 μg/mL ICG. At 1, 4, 8, 12, 24, and 48 h postinjection, the mice were subjected to fluorescence imaging under an IVIS Spectrum imaging system (Perkin Elmer) (E_x: 745 nm; E_m: 840 nm). These mice were also observed for photoacoustic imaging using a MSOT inVision 256-TF small animal imaging system (iThera Medical GmbH, Munich, Germany). After 24 h postinjection of nanoparticles, the mice were sacrificed to extract major organs (liver, spleen, kidneys, heart, and lungs) and tumors. Ex vivo fluorescence imaging was carried out through the IVIS Spectrum imaging system (Perkin Elmer) for semiquantitative biodistribution analysis.

As for in vivo MRI experiments, A549 xenografted tumor mice were intravenously injected with 200 μL of 20 mg/mL AM-PP@ICGNPs and bare PP@ICGNPs. At 24 h postinjection, MRI measurements were carried out on a 9.4 T Micro-imaging system (Bruker Avance 400, Ettlingen, Germany). A 5 mm NMR tube containing 300 μL of PP@ICGNP solution (C_F = 46 mM) was placed on the side of nude mice and applied as the external reference. After in vivo ^{19}F MRI assays, the mice were sacrificed, and tumors were extracted and smashed. The smashed tumors were suspended in PBS and the concentration was adjusted to 14 mg/mL. Later, 250 μL of the tumor suspension plus 250 μL of 1 mM CF_3SO_3Na (internal reference) were put into an NMR tube; ^{19}F NMR measurements were carried out on a 500 MHz spectrometer.

In Vivo Photothermal Effect of AM-PP@ICGNPs. A549 xenografted tumor mice were intravenously injected with 200 μL of AM-PP@ICGNPs and bare PP@ICGNPs with a concentration of 500 μg/mL of ICG. Mice were anesthetized after 24 h of injection, and a 765 nm NIR laser (400 mW/cm^2) was employed to illuminate tumor sites for 15 min. Tumor surface temperatures were recorded using an infrared imaging device.

In Vivo Antitumor Efficacy of AM-PP@ICGNPs. When the tumors had grown to about 0.4 cm in diameter, twenty mice were averagely allocated into four groups. The mice were treated with 200 μL of PBS, ICG (500 μg/mL), PP@ICGNPs (500 μg/mL of ICG), and AM-PP@ICGNPs (500 μg/mL of ICG) through tail vein injection. After 24 h of injection, a 765 nm NIR laser (400 mW/cm^2) was employed to illuminate tumor sites for 15 min. Treatment was given once every 6 days for a total of three times.

The nude mice weights were recorded every 6 days and the tumor volume was measured. The tumor volume (V) is determined through the following formula: $V = \sum$ slice area × slice thickness. The MRI image of the transverse section of the tumor was recorded; the slice area, slice thickness, and volume of each tumor layer were determined and were added up.

■ ASSOCIATED CONTENT

Supporting Information

The Supporting Information is available free of charge at https://pubs.acs.org/doi/10.1021/acsami.0c13865.

Experimental methods; the standard curve of the UV−vis absorption spectrum of ICG; DLS diameter distribution of AM vesicles, PPNPs, and AM-PPNPs; photothermal stability of AM-PP@ICGNPs; SDS-PAGE protein analysis; CLSM of A549 cells incubated with AM-PP@FITCNPs under specific times; colocalization of the A549 membranes and polymeric cores during endocytosis; blood circulation curves of ICG, PP@ICGNPs, and AM-PP@ICGNPs; histopathologic exami-

https://dx.doi.org/10.1021/acsami.0c13865
ACS Appl. Mater. Interfaces 2020, 12, 57290−57301

nation of organ tissues after photothermal therapy; blood biochemistry analysis (PDF)

AUTHOR INFORMATION

Corresponding Authors

Shizhen Chen − *Key Laboratory of Magnetic Resonance in Biological Systems, State Key Laboratory of Magnetic Resonance and Atomic and Molecular Physics, National Center for Magnetic Resonance in Wuhan, Wuhan Institute of Physics and Mathematics, Innovation Academy for Precision Measurement Science and Technology, Chinese Academy of Sciences − Wuhan National Laboratory for Optoelectronics, Wuhan 430071, P. R. China; University of Chinese Academy of Sciences, Beijing 100049, P. R. China;* Email: chenshizhen@wipm.ac.cn

Xin Zhou − *Key Laboratory of Magnetic Resonance in Biological Systems, State Key Laboratory of Magnetic Resonance and Atomic and Molecular Physics, National Center for Magnetic Resonance in Wuhan, Wuhan Institute of Physics and Mathematics, Innovation Academy for Precision Measurement Science and Technology, Chinese Academy of Sciences − Wuhan National Laboratory for Optoelectronics, Wuhan 430071, P. R. China; University of Chinese Academy of Sciences, Beijing 100049, P. R. China;* orcid.org/0000-0002-5580-7907; Email: xinzhou@wipm.ac.cn

Authors

Sha Li − *Key Laboratory of Magnetic Resonance in Biological Systems, State Key Laboratory of Magnetic Resonance and Atomic and Molecular Physics, National Center for Magnetic Resonance in Wuhan, Wuhan Institute of Physics and Mathematics, Innovation Academy for Precision Measurement Science and Technology, Chinese Academy of Sciences − Wuhan National Laboratory for Optoelectronics, Wuhan 430071, P. R. China; University of Chinese Academy of Sciences, Beijing 100049, P. R. China*

Weiping Jiang − *Key Laboratory of Magnetic Resonance in Biological Systems, State Key Laboratory of Magnetic Resonance and Atomic and Molecular Physics, National Center for Magnetic Resonance in Wuhan, Wuhan Institute of Physics and Mathematics, Innovation Academy for Precision Measurement Science and Technology, Chinese Academy of Sciences − Wuhan National Laboratory for Optoelectronics, Wuhan 430071, P. R. China; University of Chinese Academy of Sciences, Beijing 100049, P. R. China*

Yaping Yuan − *Key Laboratory of Magnetic Resonance in Biological Systems, State Key Laboratory of Magnetic Resonance and Atomic and Molecular Physics, National Center for Magnetic Resonance in Wuhan, Wuhan Institute of Physics and Mathematics, Innovation Academy for Precision Measurement Science and Technology, Chinese Academy of Sciences − Wuhan National Laboratory for Optoelectronics, Wuhan 430071, P. R. China; University of Chinese Academy of Sciences, Beijing 100049, P. R. China*

Meiju Sui − *Key Laboratory of Magnetic Resonance in Biological Systems, State Key Laboratory of Magnetic Resonance and Atomic and Molecular Physics, National Center for Magnetic Resonance in Wuhan, Wuhan Institute of Physics and Mathematics, Innovation Academy for Precision Measurement Science and Technology, Chinese Academy of Sciences − Wuhan National Laboratory for Optoelectronics, Wuhan 430071, P. R. China; University of Chinese Academy of Sciences, Beijing 100049, P. R. China*

Yuqi Yang − *Key Laboratory of Magnetic Resonance in Biological Systems, State Key Laboratory of Magnetic Resonance and Atomic and Molecular Physics, National Center for Magnetic Resonance in Wuhan, Wuhan Institute of Physics and Mathematics, Innovation Academy for Precision Measurement Science and Technology, Chinese Academy of Sciences − Wuhan National Laboratory for Optoelectronics, Wuhan 430071, P. R. China; University of Chinese Academy of Sciences, Beijing 100049, P. R. China*

Liqun Huang − *Key Laboratory of Magnetic Resonance in Biological Systems, State Key Laboratory of Magnetic Resonance and Atomic and Molecular Physics, National Center for Magnetic Resonance in Wuhan, Wuhan Institute of Physics and Mathematics, Innovation Academy for Precision Measurement Science and Technology, Chinese Academy of Sciences − Wuhan National Laboratory for Optoelectronics, Wuhan 430071, P. R. China; University of Chinese Academy of Sciences, Beijing 100049, P. R. China*

Ling Jiang − *Key Laboratory of Magnetic Resonance in Biological Systems, State Key Laboratory of Magnetic Resonance and Atomic and Molecular Physics, National Center for Magnetic Resonance in Wuhan, Wuhan Institute of Physics and Mathematics, Innovation Academy for Precision Measurement Science and Technology, Chinese Academy of Sciences − Wuhan National Laboratory for Optoelectronics, Wuhan 430071, P. R. China; University of Chinese Academy of Sciences, Beijing 100049, P. R. China*

Maili Liu − *Key Laboratory of Magnetic Resonance in Biological Systems, State Key Laboratory of Magnetic Resonance and Atomic and Molecular Physics, National Center for Magnetic Resonance in Wuhan, Wuhan Institute of Physics and Mathematics, Innovation Academy for Precision Measurement Science and Technology, Chinese Academy of Sciences − Wuhan National Laboratory for Optoelectronics, Wuhan 430071, P. R. China; University of Chinese Academy of Sciences, Beijing 100049, P. R. China;* orcid.org/0000-0002-9359-915X

Complete contact information is available at: https://pubs.acs.org/10.1021/acsami.0c13865

Notes

The authors declare no competing financial interest.

ACKNOWLEDGMENTS

This work is supported by the National Key R&D Program of China (2018YFA0704000), the National Natural Science Foundation of China (81625011, 91859206, 21921004, and 21874150), the Key Research Program of Frontier Sciences, CAS (ZDBS-LY-JSC004 and QYZDY-SSW-SLH018), the Youth Innovation Promotion Association of the Chinese Academy of Sciences (2018365), and Hubei Provincial Natural Science Foundation of China (2017CFA013 and 2018ACA143). Xin Zhou acknowledges the support from the Tencent Foundation through the XPLORER PRIZE.

REFERENCES

(1) Kelkar, S. S.; Reineke, T. M. Theranostics: Combining Imaging and Therapy. *Bioconjugate Chem.* **2011**, *22*, 1879−1903.

(2) Lee, D. E.; Koo, H.; Sun, I. C.; Ryu, J. H.; Kin, K.; Kwon, I. C. Multifunctional nanoparticles for multimodal imaging and theragnosis. *Chem. Soc. Rev.* **2012**, *41*, 2656−2672.

(3) Yang, Y. Q.; Chen, S. Z.; Liu, L. H.; Li, S.; Zeng, Q. B.; Zhu, X. L.; Li, H. D.; Zhang, Z. Y.; Bouchard, L. S.; Liu, M. L.; Zhou, X.

Increasing Cancer Therapy Efficiency through Targeting and Localized Light Activation. *ACS Appl. Mater. Interfaces* **2017**, *9*, 23400−23408.
(4) Wu, S. Q.; Qiao, Z. H.; Li, Y.; Hu, S. P.; Ma, Y.; Wei, S. Y.; Zhang, L. B. Persistent Luminescence Nanoplatform with Fenton-like Catalytic Activity for Tumor Multimodal Imaging and Photoenhanced Combination Therapy. *ACS Appl. Mater. Interfaces* **2020**, *12*, 25572−25580.
(5) Zhang, Y. F.; Bo, S. W.; Feng, T.; Qin, X. L.; Wan, Y. L.; Jiang, S. S.; Li, C. X.; Lin, J.; Wang, T. F.; Zhou, X.; Jiang, Z. X.; Huang, P. A Versatile Theranostic Nanoemulsion for Architecture- Dependent Multimodal Imaging and Dually Augmented Photodynamic Therapy. *Adv. Mater.* **2019**, *31*, No. 1806444.
(6) Smith, B. R.; Gambhir, S. S. Nanomaterials for In Vivo Imaging. *Chem. Rev.* **2017**, *117*, 901−986.
(7) Terreno, E.; Castelli, D. D.; Viale, A.; Aime, S. Challenges for Molecular Magnetic Resonance Imaging. *Chem. Rev.* **2010**, *110*, 3019−3042.
(8) Angelovski, G. What We Can Really Do with Bioresponsive MRI Contrast Agents. *Angew. Chem., Int. Ed.* **2016**, *55*, 7038−7046.
(9) Zhang, B. B.; Li, Q.; Yin, P. H.; Rui, Y. P.; Qiu, Y. Y.; Wang, Y.; Shi, D. L. Ultrasound- Triggered BSA/SPION Hybrid Nanoclusters for Liver-Specific Magnetic Resonance Imaging. *ACS Appl. Mater. Interfaces* **2012**, *4*, 6479−6486.
(10) Hong, G. S.; Antaris, A. L.; Dai, H. J. Near-infrared fluorophores for biomedical imaging. *Nat. Biomed. Eng.* **2017**, *1*, 1.
(11) Mallidi, S.; Luke, G. P.; Emelianov, S. Photoacoustic imaging in cancer detection, diagnosis, and treatment guidance. *Trends Biotechnol.* **2011**, *29*, 213−221.
(12) Wu, M. L.; Mei, T. X.; Lin, C. Y.; Wang, Y. C.; Chen, J. Y.; Le, W. J.; Sun, M. Y.; Xu, J. G.; Dai, H. Y.; Zhang, Y. F.; Xue, C. Y.; Liu, Z. M.; Chen, B. D. Melanoma Cell Membrane Biomimetic Versatile CuS Nanoprobes for Homologous Targeting Photoacoustic Imaging and Photothermal Chemotherapy. *ACS Appl. Mater. Interfaces* **2020**, *12*, 16031−16039.
(13) Lee, D.; Beack, S.; Yoo, J.; Kim, S. K.; Lee, C.; Kwon, W.; Hahn, S. K.; Kim, C. In Vivo Photoacoustic Imaging of Livers Using Biodegradable Hyaluronic Acid-Conjugated Silica Nanoparticles. *Adv. Funct. Mater.* **2018**, *28*, No. 1800941.
(14) Liu, L. H.; Yuan, Y. P.; Yang, Y. Q.; McMahon, M. T.; Chen, S. Z.; Zhou, X. A fluorinated aza-BODIPY derivative for NIR fluorescence/PA/^{19}F MR tri-modality in vivo Imaging. *Chem. Commun.* **2019**, *55*, 5851−5854.
(15) Hu, X. M.; Tang, Y. F.; Hu, Y. X.; Lu, F.; Lu, X. M.; Wang, Y. Q.; Li, J.; Li, Y. Y.; Ji, Y.; Wang, W. J.; Ye, D. J.; Fan, Q. L.; Huang, W. Gadolinium Chelated Conjugated Polymer-Based Nanotheranostics for Photoacoustic/Magnetic Resonance/NIR-II Fluorescence Imaging-Guided Cancer Photothermal Therapy. *Theranostics* **2019**, *9*, 4168−4181.
(16) Liu, Y.; Kang, N.; Lv, J.; Zhou, Z. J.; Zhao, Q. L.; Ma, L. C.; Chen, Z.; Ren, L.; Nie, L. M. Deep Photoacoustic/Luminescence/Magnetic Resonance Multimodal Imaging in Living Subjects Using High Efficiency Upconversion Nanocomposites. *Adv. Mater.* **2016**, *28*, 6411−6419.
(17) Caravan, P.; Ellison, J. J.; McMurry, T. J.; Lauffer, R. B. Gadolinium(III) Chelates as MRI Contrast Agents: Structure, Dynamics, and Applications. *Chem. Rev.* **1999**, *99*, 2293−2352.
(18) Taylor, K. M. L.; Kim, J. S.; Rieter, W. J.; An, H. Y.; Lin, W. L.; Lin, W. B. Mesoporou Silica Nanospheres as Highly Efficient MRI Contrast Agents. *J. Am. Chem. Soc.* **2008**, *130*, 2154−2155.
(19) Manus, L. M.; Mastarone, D. J.; Waters, E. A.; Zhang, X. Q.; Schultz-Sikma, E. A.; MacRenaris, K. W.; Ho, D.; Meade, T. J. Gd(III)-Nanodiamond Conjugates for MRI Contrast Enhancement. *Nano Lett.* **2010**, *10*, 484−489.
(20) Zhao, Z. L.; Fan, H. H.; Zhou, G. F.; Bai, H. R.; Liang, H.; Wang, R. W.; Zhang, X. B.; Tan, W. H. Activatable Fluorescence/MRI Bimodal Platform for Tumor Cell Imaging via MnO_2 Nanosheet−Aptamer Nanoprobe. *J. Am. Chem. Soc.* **2014**, *136*, 11220−11223.
(21) Wei, H.; Bruns, O. T.; Kaul, M. G.; Hansen, E. C.; Barch, M.; Wisniowska, A.; Chen, O.; Chen, Y.; Li, N.; Okada, S.; Cordero, J. M.; Heine, M.; Farrar, C. T.; Montana, D. M.; Adam, G.; Ittrich, H.; Jasanoff, A.; Nielsen, P.; Bawendi, M. G. Exceedingly small iron oxide nanoparticles as positive MRI contrast agents. *Proc. Natl. Acad. Sci. USA* **2017**, *114*, 2325−2330.
(22) Bulte, J. W. M.; Kraitchman, D. L. Iron oxide MR contrast agents for molecular and cellular imaging. *NMR Biomed.* **2004**, *17*, 484−499.
(23) Na, H. B.; Song, I. C.; Hyeon, T. Inorganic Nanoparticles for MRI Contrast Agents. *Adv. Mater.* **2009**, *21*, 2133−2148.
(24) Tassa, C.; Shaw, S. Y.; Weissleder, R. Dextran-Coated Iron Oxide Nanoparticles: A Versatile Platform for Targeted Molecular Imaging, Molecular Diagnostics, and Therapy. *Acc. Chem. Res.* **2011**, *44*, 842−852.
(25) Wang, L. Y.; Huang, J.; Chen, H. B.; Wu, H.; Xu, Y. L.; Li, Y. C.; Yi, H.; Wang, Y. A.; Yang, L.; Mao, H. Exerting Enhanced Permeability and Retention Effect Driven Delivery by Ultrafine Iron Oxide Nanoparticles with T1−T2 Switchable Magnetic Resonance Imaging Contrast. *ACS Nano* **2017**, *11*, 4582−4592.
(26) Ruiz-Cabello, J.; Barnett, B. P.; Bottomley, P. A.; Bulte, J. W. M. Fluorine (^{19}F) MRS and MRI in biomedicine. *NMR Biomed.* **2011**, *24*, 114−129.
(27) Huang, P. S.; Guo, W. S.; Yang, G.; Song, H. J.; Wang, Y. Q.; Wang, C.; Kong, D. L.; Wang, W. W. Fluorine Meets Amine: Reducing Microenvironment-Induced Amino-Activatable Nanoprobes for ^{19}F-Magnetic Resonance Imaging of Biothiols. *ACS Appl. Mater. Interfaces* **2018**, *10*, 18532−18542.
(28) Guo, Z. D.; Gao, M. N.; Song, M. L.; Li, Y. S.; Zhang, D. L.; Xu, D.; You, L. Y.; Wang, L. L.; Zhuang, R. Q.; Su, X. H.; Liu, T.; Du, J.; Zhang, X. Z. Superfluorinated PEI Derivative Coupled with 99mTc for ASGPR Targeted 19F MRI/SPECT/PA Tri-Modality Imaging. *Adv. Mater.* **2016**, *28*, 5898−5906.
(29) Yuan, Y.; Ge, S. C.; Sun, H. B.; Dong, X. J.; Zhao, H. X.; An, L. N.; Zhang, J.; Wang, J. F.; Hu, B.; Liang, G. L. Intracellular Self-Assembly and Disassembly of ^{19}F Nanoparticles Confer Respective "Off" and "On" ^{19}F NMR/MRI Signals for Legumain Activity Detection in Zebrafish. *ACS Nano* **2015**, *9*, 5117−5124.
(30) Tirotta, I.; Dichiarante, V.; Pigliacelli, C.; Cavallo, G.; Terraneo, G.; Bombelli, F. B.; Metrangolo, P.; Resnati, G. ^{19}F Magnetic Resonance Imaging (MRI): From Design of Materials to Clinical Applications. *Chem. Rev.* **2015**, *115*, 1106−1129.
(31) Bose, T.; Latawiec, D.; Mondal, P. P.; Mandal, S. Overview of nano-drugs characteristics for clinical application: the journey from the entry to the exit point. *J. Nanopart. Res.* **2014**, *16*, 2527.
(32) Li, R. X.; He, Y. W.; Zhang, S. Y.; Qin, J.; Wang, J. X. Cell membrane-based nanoparticles: a new biomimetic platform for tumor diagnosis and treatment. *Acta Pharm. Sin. B* **2018**, *8*, 14−22.
(33) Yan, H. Z.; Shao, D.; Lao, Y-H.; Li, M. Q.; Hu, H. Z.; Leong, K. W. Engineering Cell Membrane-Based Nanotherapeutics to Target Inflammation. *Adv. Sci.* **2019**, *6*, No. 1900605.
(34) Hu, C.-M. J.; Zhang, L.; Aryal, S.; Cheung, C.; Fang, R. H.; Zhang, L. F. Erythrocyte membrane-camouflaged polymeric nanoparticles as a biomimetic delivery platform. *Proc. Natl. Acad. Sci. USA* **2011**, *108*, 10980−10985.
(35) Gao, W. W.; Hu, C-M. J.; Fang, R. H. B.; Luk, T.; Su, J.; Zhang, L. F. Surface Functionalization of Gold Nanoparticles with Red Blood Cell Membranes. *Adv. Mater.* **2013**, *25*, 3549−3553.
(36) Su, J. H.; Sun, H. P.; Meng, Q. S.; Yin, Q.; Tang, S.; Zhang, P. C.; Chen, Y.; Zhang, Z. W.; Yu, H. J.; Li, Y. P. Long Circulation Red-Blood-Cell-Mimetic Nanoparticles with Peptide-Enhanced Tumor Penetration for Simultaneously Inhibiting Growth and Lung Metastasis of Breast Cancer. *Adv. Funct. Mater.* **2016**, *26*, 1243−1252.
(37) Peng, J. R.; Yang, Q.; Li, W. T.; Tan, L. W.; Xiao, Y.; Chen, L. J.; Hao, Y.; Qian, Z. Y. Erythrocyte-Membrane-Coated Prussian Blue/Manganese Dioxide Nanoparticles as H_2O_2- Responsive Oxygen Generators To Enhance Cancer Chemotherapy/Photothermal Therapy. *ACS Appl. Mater. Interfaces* **2017**, *9*, 44410−44422.

https://dx.doi.org/10.1021/acsami.0c13865
ACS Appl. Mater. Interfaces 2020, 12, 57290−57301

(38) Toledano Furman, N. E.; Haber, Y. L.; Bronshtein, T.; Kaneti, L.; Letko, N.; Weinstein, E.; Baruch, L.; Machluf, M. Reconstructed Stem Cell Nanoghosts: A Natural Tumor Targeting Platform. *Nano Lett.* **2013**, *13*, 3248−3255.
(39) Han, Y. Y.; Pan, H.; Li, W. J.; Chen, Z.; Ma, A. Q.; Yin, T.; Liang, R. J.; Chen, F. M.; Ma, Y. F.; Jin, Y.; Zheng, M. B.; Li, B. H.; Cai, L. T. T Cell Membrane Mimicking Nanoparticles with Bioorthogonal Targeting and Immune Recognition for Enhanced Photothermal Therapy. *Adv. Sci.* **2019**, *6*, No. 1900251.
(40) Deng, G. J.; Sun, Z. H.; Li, S. P.; Peng, X. H.; Li, W. J.; Zhou, L. H.; Ma, Y. F.; Gong, P.; Cai, L. T. Cell-Membrane Immunotherapy Based on Natural Killer Cell Membrane Coated Nanoparticles for the Effective Inhibition of Primary and Abscopal Tumor Growth. *ACS Nano* **2018**, *12*, 12096−12108.
(41) Bose, R. J. C.; Paulmurugan, R.; Moon, J.; Lee, S. H.; Park, H. Cell membrane-coated nanocarriers: the emerging targeted delivery system for cancer theranostics. *Drug Discovery Today* **2018**, *23*, 891−899.
(42) Chen, Z.; Zhao, P. F.; Luo, Z. Y.; Zheng, M. B.; Tian, H.; Gong, P.; Gao, G. H.; Pan, H.; Liu, L. L.; Ma, A. Q.; Cui, H. D.; Ma, Y. F.; Cai, L. T. Cancer Cell Membrane Biomimetic Nanoparticles for Homologous-Targeting Dual-Modal Imaging and Photothermal Therapy. *ACS Nano* **2016**, *10*, 10049−10057.
(43) Yang, R.; Xu, J.; Xu, L. G.; Sun, X. Q.; Chen, Q.; Zhao, Y. H.; Peng, R.; Liu, Z. Cancer Cell Membrane-Coated Adjuvant Nanoparticles with Mannose Modification for Effective Anticancer Vaccination. *ACS Nano* **2018**, *12*, 5121−5129.
(44) Gao, M.; Liang, C.; Song, X. J.; Chen, Q.; Jin, Q. T.; Wang, C.; Liu, Z. Erythrocyte Membrane Enveloped Perfluorocarbon as Nanoscale Artificial Red Blood Cells to Relieve Tumor Hypoxia and Enhance Cancer Radiotherapy. *Adv. Mater.* **2017**, *29*, No. 1701429.
(45) Mitra, K.; Belandia, I. U.; Taguchi, T.; Warren, G.; Engelman, D. M. Modulation of the bilayer thickness of exocytic pathway membranes by membrane proteins rather than cholesterol. *Proc. Natl. Acad. Sci. USA* **2004**, *101*, 4083−4088.
(46) Zhang, C.; Moonshi, S. S.; Wang, W. Q.; Ta, H. T.; Han, Y. X.; Han, F. Y.; Peng, H.; Kra'l, P.; Rolfe, B. E.; Gooding, J. J.; Gaus, K.; Whittaker, A. K. High F-Content Perfluoropolyether-Based Nanoparticles for Targeted Detection of Breast Cancer by ^{19}F Magnetic Resonance and Optical Imaging. *ACS Nano* **2018**, *12*, 9162−9176.
(47) Goldberg, S. N.; Gazelle, G. S.; Mueller, P. R. Thermal Ablation Therapy for Focal Malignancy: A Unified Approach to Underlying Principles, Techniques, and Diagnostic Imaging Guidance. *Am. J. Roentgenol.* **2000**, *174*, 323−331.

https://dx.doi.org/10.1021/acsami.0c13865
ACS Appl. Mater. Interfaces 2020, 12, 57290−57301